RSC Advances

PAPER

View Article Online
View Journal | View Issue

Cite this: *RSC Adv.*, 2021, **11**, 32376

Chemical synthesis of $Nd_2Fe_{14}B$/Fe–Co nanocomposite with high magnetic energy product†

Hieu Minh Ngo,[a] Gyutae Lee,[b] Syed Kamran Haider,[a] Umapada Pal,[a‡] Thomi Hawari,[a] Kyung Min Kim,[c] Jongryoul Kim,[b] Hae-Woong Kwon[c] and Young Soo Kang[*a]

$Nd_2Fe_{14}B$ is one of the most popular permanent magnets (PMs) possessing the best energy product $(BH)_{max}$ among the common PM materials. However, exchange-coupled nanocomposite magnets fabricated by embedding nanostructures of soft-phase magnetic materials into a hard-phase magnetic matrix manifest higher remanence and a higher energy product. Here we present the fabrication of exchange coupled $Nd_2Fe_{14}B$/Fe–Co magnetic nanocomposites using gel-combustion and diffusion–reduction processes. Pre-fabricated $CoFe_2O_4$ nanoparticles (NPs) of ~5 nm diameter were incorporated into a Nd–Fe–B oxide matrix during its synthesis by gel-combustion. The obtained mixed oxide was further processed with oxidative annealing at 800 °C for 2 h and reductive annealing at 900 °C for 2 h to form a $Nd_2Fe_{14}B$/Fe–Co nanocomposite. Nanocomposites with different mol% of soft-phase were prepared and characterized by X-ray diffraction (XRD), transmission electron microscopy (TEM) and physical property measurement system (PPMS) to study their crystalline phase, morphology and magnetic behavior. Addition of 7.7 mol% of soft-phase was found to be optimum, producing a coercivity (H_c) of 5.6 kOe and remanence (M_r) of 54 emu g^{-1} in the nanocomposite.

Received 14th May 2021
Accepted 17th September 2021

DOI: 10.1039/d1ra03760a

rsc.li/rsc-advances

Introduction

Rare-earth based permanent magnets are an indispensable part of modern life with applications spanning from actuators to motors, sensors to computer hard disk drives, to mention a few. However, the limited abundance of rare-earth elements in the earth is a hindrance to coping with the growing demand for these materials.[1,2] To meet the world demand, researchers are looking for alternative methods such as recycling[3] or other materials that are cheaper and capable of storing high energy to replace conventional rare-earth-based permanent magnets.[4] One of the attempts is fabricating the permanent magnets with another soft magnetic material, using the exchange coupling interaction[5,6] between the respective hard and soft magnetic domains. Exchange coupled magnets, which are basically the composites of hard rare-earth-based magnetic particles and rare-earth free soft magnetic particles, have been predicted to have larger energy product $(BH)_{max}$ as the consequence of high magnetization of the soft-magnetic particles and high coercivity of the hard-magnetic particles.[6–10] For example, nanocomposite of $Sm_2Fe_{17}N_3$ and $Fe_{65}Co_{35}$ containing only 9 vol% hard phase ($Sm_2Fe_{17}N_3$) has been theoretically predicted to have highest $(BH)_{max}$ value of 137 MGOe.[5] Many attempts have been made to synthesize these new type of magnetic materials using different methods during the last 12 years.[11–20] Utilizing magnetron sputtering, Cui *et al.* fabricated $Nd_2Fe_{14}B$/Ta/$Fe_{67}Co_{33}$ anisotropic nanocomposite films which manifested $(BH)_{max}$ value as high as 60 MGOe.[11] Using a chemical method, Hou *et al.* synthesized $SmCo_5$/α-Fe nanocomposite with a coercivity of 6.05 kOe and magnetic remanence of 56 emu g^{-1}.[12] On the other hand, Shen *et al.* prepared exchange-coupled $SmCo_5$/α-Fe magnetic nanocomposite with 13.2 kOe coercivity (H_c) and 61.5 emu g^{-1} remanence (M_r).[13] Utilizing a reduction–diffusion process, Yu *et al.* fabricated exchange-coupled $Nd_2Fe_{14}B$/α-Fe nanocomposite by dispersing α-Fe nanoparticles (NPs) into Nd–Fe–B matrix. The magnetic nanocomposite revealed a coercivity of 12 kOe and remanence of 45 emu g^{-1}.[14] However, the same nanocomposite prepared by Zhong *et al.* through microwave-assisted combustion process produced H_c = 9 kOe and M_r = 110 emu g^{-1}.[16] The results presented above indicate the performance of exchange coupled magnetic nanocomposites

[a]*Department of Chemistry, Sogang University, #1 Shinsu-dong, Mapo-gu, Seoul 121-742, Republic of Korea. E-mail: yskang@sogang.ac.kr*

[b]*Department of Materials Science & Chemical Engineering, Hanyang University, #320, 55, Hanyangdaehak-ro, Sangnok-gu, Ansan, Kyeonggi-do, 426-791, Republic of Korea*

[c]*Department of Materials Science and Engineering, Pukyong National University, Busan, 48513, Republic of Korea*

† Electronic supplementary information (ESI) available: Containing details of materials and experimental methods, additional supporting data such as structural (XRD), microscopic (SEM, TEM) and composition analysis (EDS) of the nanocomposites. See DOI: 10.1039/d1ra03760a

‡ On leave from Instituto of Physics, Autonomous University of Puebla, Mexico.

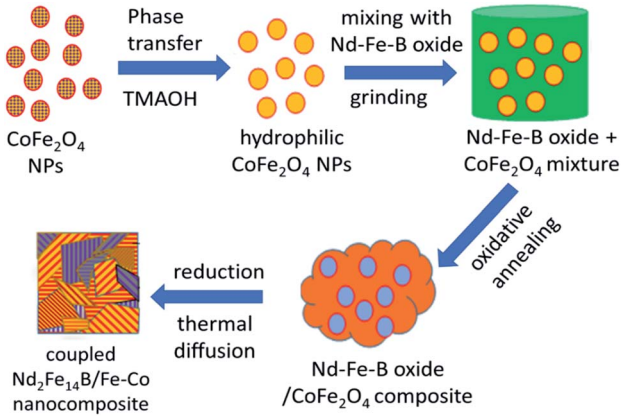

Fig. 1 Schematic presentation of the sequential steps of fabricating $Nd_2Fe_{14}B$/Co–Fe exchange-coupled nanocomposite.

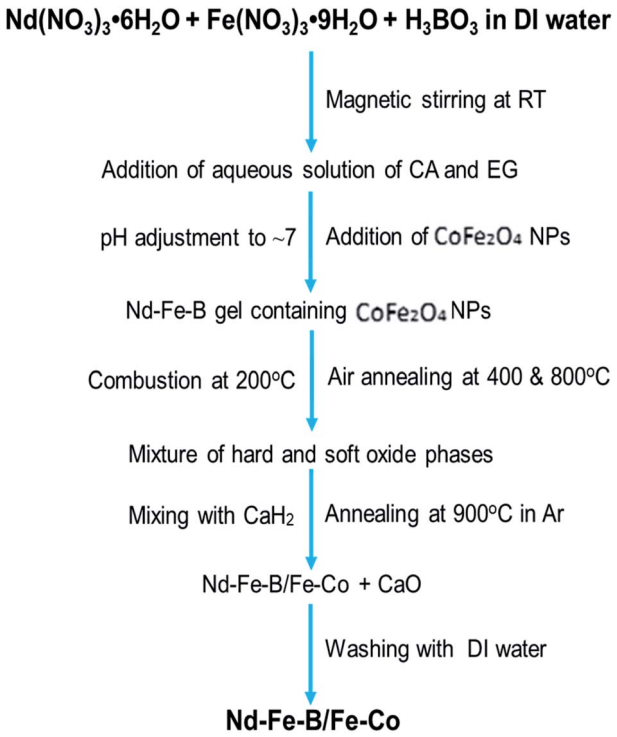

Fig. 2 Flow chart of the processing steps used for the synthesis of exchange coupled Nd–Fe–B/Fe–Co nanocomposites.

strongly depends on their fabrication method, which controls their morphology, grain size, extent of inter-diffusion of hard- and soft-phase grains (fusion of grain boundary), and the volume fraction of the soft magnetic phase.

Herein, we present the fabrication of $Nd_2Fe_{14}B$/Fe–Co nanocomposites through a reduction–diffusion process. The magnetic nanocomposites were prepared by dispersing different mol% of $CoFe_2O_4$ (Fe–Co oxide) nanoparticles (NPs) of ~5 nm average size in Nd–Fe–B oxide matrix and subsequent thermal annealing in reducing atmosphere. The ratio of soft and hard phase in the composite was varied to obtain optimum coercivity (H_c) and magnetic remanence (M_r). Finally, the oxide composites were reduced by CaH_2 at 900 °C to form Nd–Fe–B/Fe–Co nanocomposites. The synthesis process utilized to fabricate the exchange-coupled nanocomposites is schematically depicted in Fig. 1.

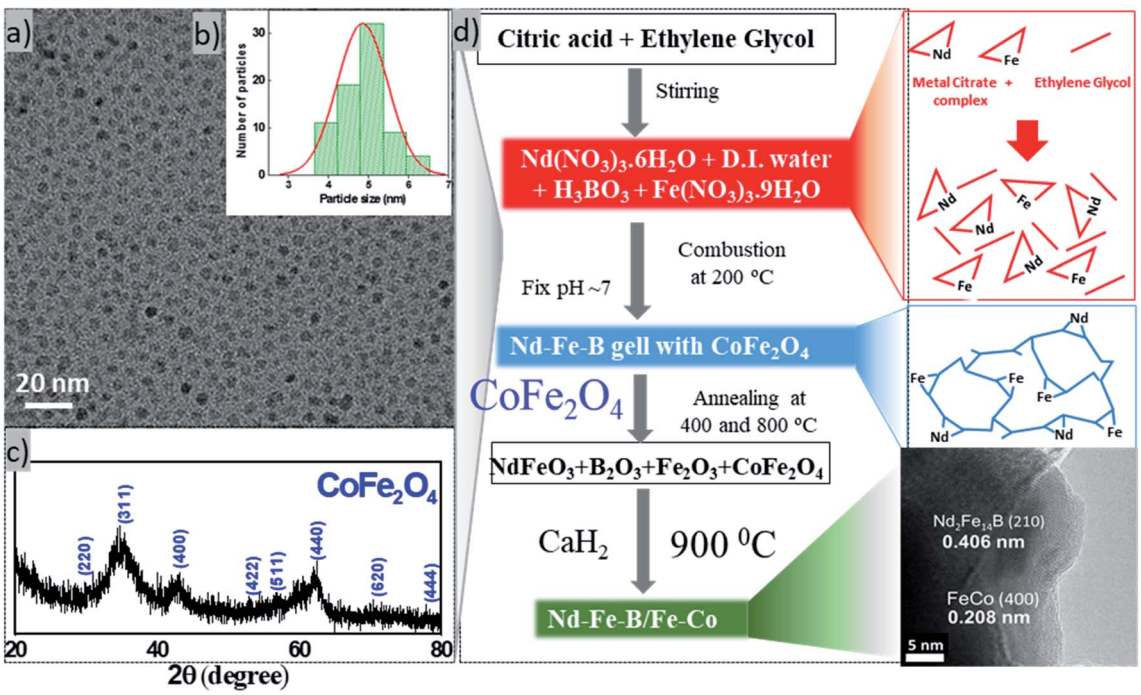

Fig. 3 (a) A typical TEM image, (b) particle size distribution, and (c) XRD pattern of the fabricated cobalt ferrite NPs. Gaussian fit to the size distribution histogram revealed ~5 nm average size of the particles. A typical optical image of sol–gel combustion synthesis procedure shown in (d).

Results and discussion

Exchange coupling across the grain boundaries between hard and soft phases leads to an enhanced remanence compared to the decoupled single-domain grains due to spin rotation in the grain boundary region. The effect was seen to increase with the decrease of grain size.[2] According to the spin-exchange coupling theory,[5] the size of the soft phase magnetic particles should be smaller than twice of the domain wall thickness of the hard phase particles to maximize the exchange coupling effect. As the domain wall thickness of hard phase Nd–Fe–B is about 3.5 nm,[21] the ideal size of the soft phase particles should be less than 7 nm. In this work, we fabricated Fe–Co NPs of ~5 nm average diameter to incorporate them into Nd–Fe–B matrix of hard phase. The complete flow chart of the process adopted for fabricating magnetic spin exchange-coupled magnetic nanocomposites has been presented in Fig. 2.

Typical TEM image, particle size distribution, and XRD pattern of the fabricated cobalt ferrite nanoparticles are presented in Fig. 3. As can be seen, the as-synthesized cobalt–ferrite nanoparticles are well dispersed, with an average size ~4.85 nm ± 0.7 nm (Fig. 3a, b and S2†). XRD pattern of the nanostructures (Fig. 3c) corresponds well with crystalline $CoFe_2O_4$ [PDF# 22-1086] in cubic phase with space group *Fd3m*. However, due to small size of the particles, the diffraction bands are broad and of low intensity. Instead of Fe–Co bimetallic nanoparticles, we fabricated cobalt ferrite nanoparticles of desired size intentionally to mix them with the hard phase Nd–Fe–B, as the oxide of bimetallic Fe–Co alloy is more stable in air than the alloy itself.[22] As the cobalt ferrite NPs were synthesized in organic solvent using organic surfactants, they had a hydrophobic surface. For their good dispersion in the aqueous hard phase precursor solution, they were treated with TMAOH, which is a common phase-transfer agent.[23] After treating with TMAOH, the cobalt ferrite particles dispersed well in water (Fig. S2d†). Now the surface-modified cobalt ferrite particles are ready to mix with Nd–Fe–B gel in the water phase. Later, the cobalt ferrite was converted to Fe–Co alloy in the reduction–diffusion step (Fig. 3d).

Nd–Fe–B oxide particles were synthesized by gel-combustion method.[24,25] This method was chosen because it is a simple, cheap, and high yield technique. In this method, nitrate salts were used as precursors. The addition of citric acid and ethylene glycol created a metal salts network, making the distribution of the elements homogeneous. Ammonia solution was added to adjust the pH of the reaction solution to 7. The added ammonia solution combined with NO_3^- anions in the solution forms NH_4NO_3, which acts as a fuel for the combustion of the precursor gel at 200 °C, producing the metal oxide.[26–28]

Fig. 4 shows the SEM, TEM and XRD patterns of $(100 - x)$% Nd–Fe–B oxide/x% Fe–Co oxide samples with increasing x values (x = 0.0–26.9 mol%) after annealing at 800 °C. The appearance of well-defined intense diffraction peaks in the diffraction patterns indicates the formation of well-crystalline grains in the samples after air-annealing at 800 °C (Fig. 4a–d). As can be noticed, XRD patterns of the nanocomposites revealed diffraction peaks of both $NdFeO_3$ (PDF# 01-082-2421) and Fe_2O_3 (PDF# 01-084-0308). As the mol percentage of the soft phase in oxide composite increased, the relative intensity of the peaks corresponds to Fe_2O_3 increased gradually (Fig. 4e and S1, ESI†). The formation of $NdFeO_3$ and Fe_2O_3 is necessary for the reduction process. While the free energy change in the reduction of Nd_2O_3 to Nd at 900 K is theoretically calculated to be around 94.465 kJ mol^{-1}, reported change in free energy for the reduction of $NdFeO_3$ to Nd + Fe by CaH_2 at same temperature is around −349.3 kJ mol^{-1}, which indicates the $NdFeO_3$ phase is easier to be reduced in the used co-reduction process than Nd_2O_3 (Table S2†).[26,27] As can be seen in Fig. 4b–d, the Nd–Fe–B oxide consists of single crystal domains of $NdFeO_3$ and Fe_2O_3 of different sizes, connected each other to form a net matrix.[29] Porous structure can be seen clearly in the SEM and TEM

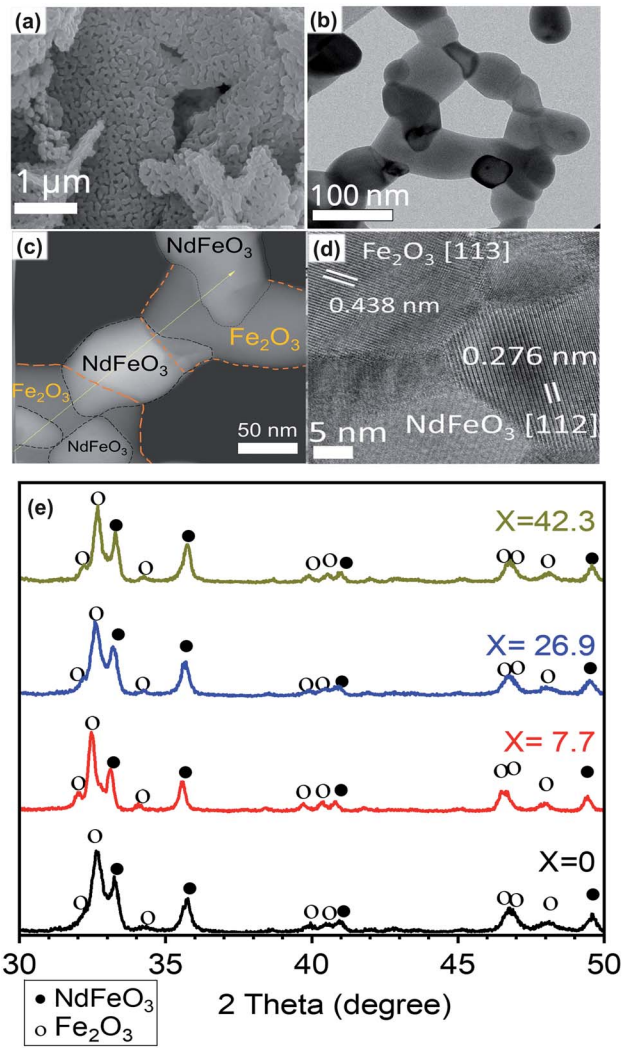

Fig. 4 SEM image (a), TEM image (b), HAADF image (c). HRTEM (d) of NdFeB-oxide (e) XRD patterns of the oxide composites containing different amounts of soft-phase oxide, and typical TEM images of Nd–Fe–B oxide, 92.3 mol% Nd–Fe–B oxide/7.7 mol% Fe–Co oxide, 90.5 mol% Nd–Fe–B oxide/9.5 mol% Fe–Co oxide, 73.1 mol% Nd–Fe–B/26.9 mol% Fe–Co oxide, 57.7 mol% Nd–Fe–B/42.3 mol% Fe–Co oxide composites. All the samples were air-annealed at 800 °C for 2 h.

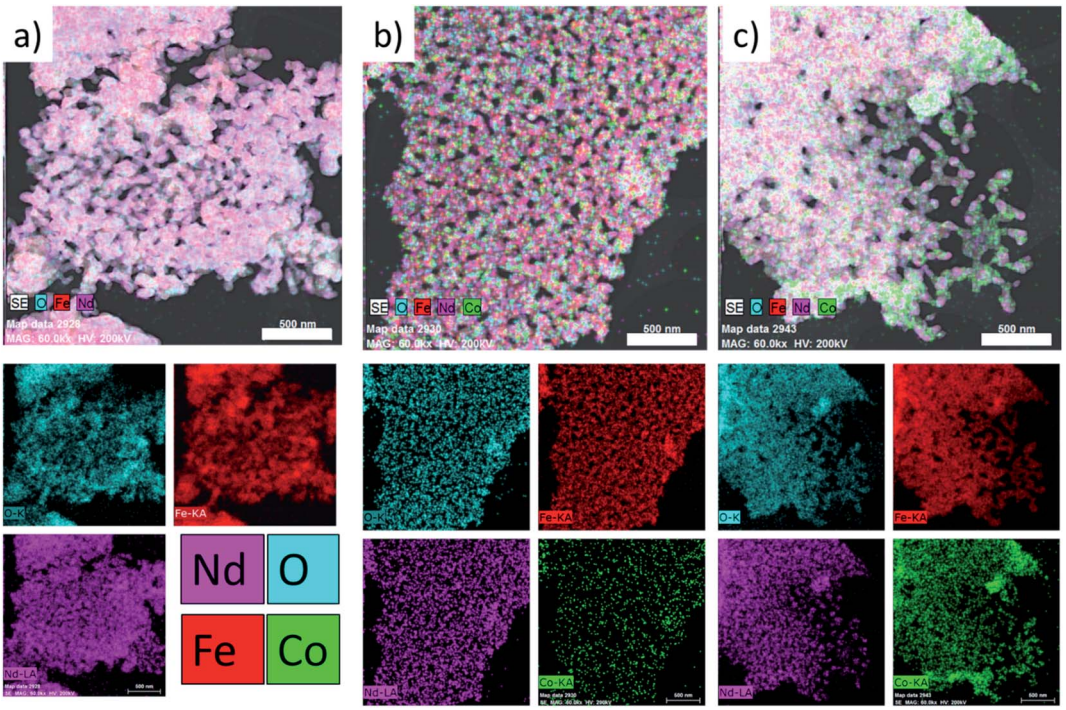

Fig. 5 EDS elemental mappings images of the (a) Nd–Fe–B oxide (with no Fe–Co oxide), (b) 92.3% Nd–Fe–B oxide/7.7% Fe–Co oxide, and (c) 73.1% Nd–Fe–B oxide/26.9% Fe–Co oxide samples after air-annealing at 800 °C for 2 h (scale bar 500 nm).

images (Fig. S3†). Absence of diffraction peak associated to boron in the XRD pattern of the oxide composites might be due to its amorphous form or low content, below the detectable limit of the diffractometer.

As can be seen in Fig. 5, the elements are distributed homogeneously in Nd–Fe–B oxide (containing no cobalt ferrite) (Fig. 5a). On the other hand, the non-uniform color contrast in the reconstructed images of the mixed oxide composite samples (Fig. 5(b and c)) clearly indicates their non-homogeneous element distribution. Inhomogeneous element distribution is even clearer in the Co mapping image (Fig. 5c) of the samples with higher soft-phase (Fe–Co oxide) contents. In fact, the distributions of Co and Nd are noticeably uneven, apparently segregated into specific regions of the composite containing high Fe–Co oxide content (Fig. 5c). It suggests a higher soft-phase oxide content could suppress the inter-diffusion process between two (soft and hard) magnetic phases. Such a non-homogeneous Co distribution in the hard–soft oxide composite, especially of high cobalt ferrite contents, is expected as the melting point of cobalt ferrite (>1500 °C)[30] is considerably higher than the melting point of Nd–Fe–B oxide (>1000 °C)[30] which suppresses the inter-diffusion of crystalline grains of the two magnetic phases.

After air-annealing, the composite oxide powders were mixed with CaH_2 and compressed into a pellet for reduction–diffusion treatment. Calcium hydride was chosen as the reducing agent because of its stronger reducing character compared to $NaBH_4$ and H_2. As has been reported in the literature, the use of $NaBH_4$ (ref. 29 and 31) or hydrogen[32] as a reducing agent in the reduction–diffusion process does not yield $Nd_2Fe_{14}B$ in high proportion as a reduction product. In fact, due to the high negative reduction potential (−2.323 eV) of Nd, it needs a strong reducing agent such as CaH_2 for a complete reduction of Nd–Fe–B oxide. More detail of thermodynamical calculation for the reduction–diffusion reaction was presented in Tables S2 and S3.†[26,27,33,34] On the other hand, the amount of CaH_2 has a critical effect on the Nd–Fe–B oxide reduction process.[26–28] While a lower CaH_2 content in the reduction mixture causes an incomplete reduction of the hard-phase oxide (leaving Nd–Fe–B oxide as a by-product), use of CaH_2 in excess although reduces the oxide completely, it leaves excess CaH_2 as an impurity in the sample, resulting in the poor magnetic property of the final product.

During washing the product with water, while the oxidized CaH_2 (*i.e.* CaO) gets dissolved to form $Ca(OH)_2$, the excess CaH_2 reacts with water, releasing hydrogen gas. The produced hydrogen gas molecules could be adsorbed on the surface of $Nd_2Fe_{14}B$ and react to form its hydride ($Nd_2Fe_{14}BH_{2x}$) (eqn (1) & (2)). As this hydride phase has low coercivity, it suppressed the magnetic properties of the fabricated $Nd_2Fe_{14}B$ nanostructures adversely.[26–28]

$$CaO + H_2O = Ca(OH)_2 + H_2 \quad (1)$$

$$Nd_2Fe_{14}B + xH_2 = Nd_2Fe_{14}BH_{2x} \quad (2)$$

Hence, we used a 1.05 : 1 ratio of CaH_2 and oxide composite sample, which was found most proper after the optimization process. The metal oxide was mixed and ground with CaH_2, then shaped into a pellet under Ar atmosphere (inside a glove

box). Compressed pellet samples have been seen to enhance the efficiency of the reduction process due to the intimate contact of the reducing agent (CaH_2) with Nd–Fe–B oxide grains.[27] After washing, the coercivity reduced a little while the remanence significantly increase, denote the effective of the reducing and washing process (Fig. S12†).

Fig. 6a shows the XRD patterns of magnetic nanocomposites prepared by reduction–diffusion treatment (at 900 °C, 2 h). The diffraction peaks revealed by the magnetic nanocomposites correspond well with the standard diffraction bands of crystalline $Nd_2Fe_{14}B$ in the tetragonal phase ($P4_2/mnm$ space group, PDF# 01-070-1385). There is no diffraction peak associated either with cobalt ferrite, Fe–Co alloy, or metallic Co in the diffraction patterns even for high concentrations (up to 26.9 mol%) of cobalt ferrite in the pelletized hard–soft oxide mixture (see Fig. S1†).

Fig. 6b showed an HRTEM image of NdFeB nanoparticles after reduction with CaH_2. As can be seen clearly, the particles are well crystalline, with different crystal domains. The particle appears to be polycrystalline, with each domain represent one facet. For example, $d = 0.266$ nm corresponding to $Nd_2Fe_{14}B$ (311), $d = 0.257$ nm corresponding to $Nd_2Fe_{14}B$ (204) facet. The d-spacing value and facets match with the XRD reference of $Nd_2Fe_{14}B$ (PDF#01-070-1385). A typical NdFeB grains morphology were shown in Fig. S6.†

The appearance of crystalline grains of individual components (soft and hard phases) in the HRTEM image (Fig. 6c) clearly demonstrates the presence of soft and hard phases in the composite.

Room temperature magnetization curves of the final exchange-coupled hard–soft nanocomposites are presented in Fig. 7. As can be seen, the Fe–Co metal alloy nanostructures revealed soft magnetic behavior at room temperature, with a slightly opened magnetic loop. Room temperature coercivity (H_c), remanence magnetization (M_r), and saturation magnetization (M_s) revealed for the soft-magnetic nanostructures were 0.60 kOe, 43.0 emu g^{-1}, and 152 emu g^{-1}, respectively. On the other hand, the uncoupled $Nd_2Fe_{14}B$ particles prepared by reducing the Nd–Fe–B oxide nanostructures revealed their ferromagnetic behavior at room temperature, with coercivity (H_c), remanence magnetization (M_r), and saturation magnetization (M_s) of about 3.9 kOe and 44.0 emu g^{-1} and 67.0 emu g^{-1}, respectively. The various prepared nanocomposites *via* sol–gel synthesis displayed very smooth *M–H* curves. The smooth curve might come from the well coupling between the soft phase or hard phase, but there is high chance that the soft phase diffuses well into the hard phase structure. That is in consistent with XRD when only 1 phase of $Nd_2Fe_{14}B$ were observed (Fig. 6a and S7†). The hard–soft exchange-coupled nanocomposite prepared by mixing 92.3 mol% of Nd–Fe–B and 7.7 mol% of Fe–Co revealed a coercivity of about 5.6 kOe, remanence magnetization about 54 emu g^{-1}, and M_s of about 59.0 emu g^{-1}. The coercivity of this sample is the highest among the fabricated nanocomposites. As can be noticed, the values of M_r and H_c of this nanocomposite are substantially higher than the values correspond to the uncoupled $Nd_2Fe_{14}B$ particles prepared in the present study. This could suggest the existence of spin coupling

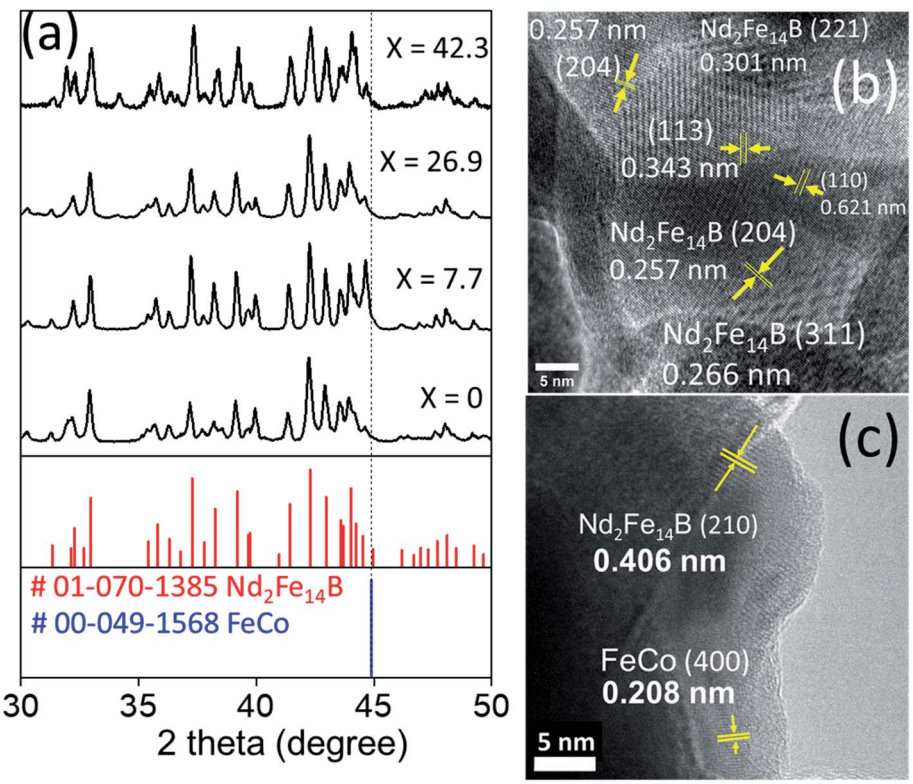

Fig. 6 (a) XRD patterns of the exchange-coupled (100 − *x*)% Nd–Fe–B/*x*% Fe–Co magnetic nanocomposites obtained after reduction–diffusion of corresponding oxide mixtures, (b) HRTEM image of NdFeB nanoparticles, (c) HRTEM image of reduced NdFeB/FeCo composite 7.7%.

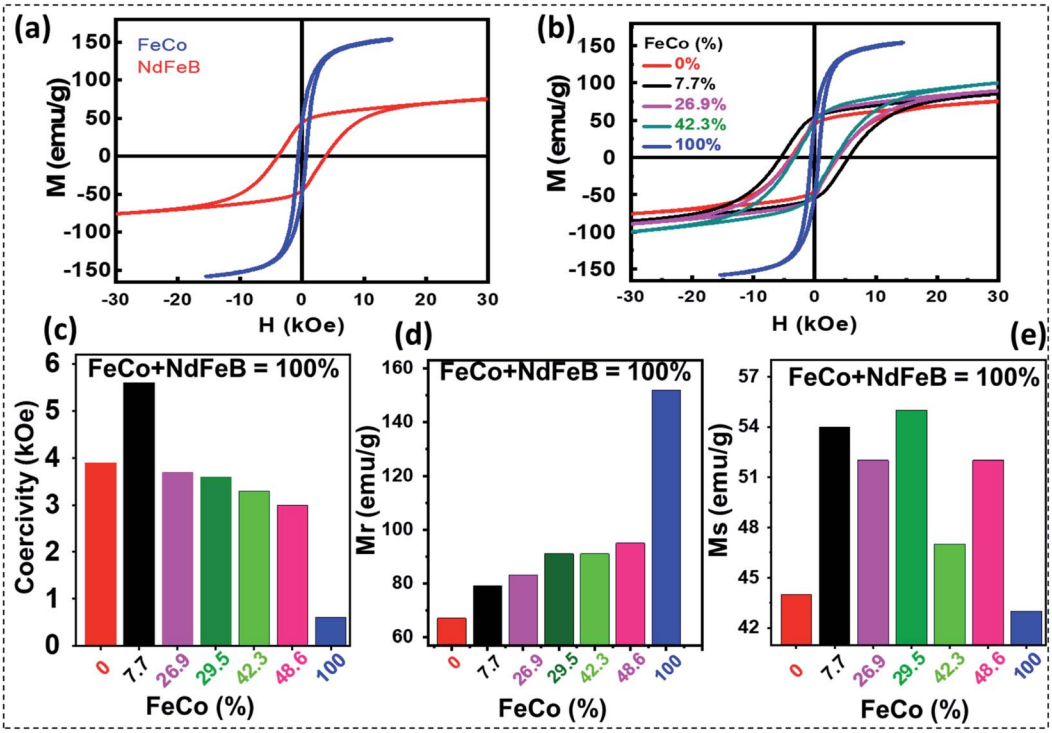

Fig. 7 (a) Room temperature $M-H$ curves of NdFeB phase and FeCo phase, (b) room temperature magnetization ($M-H$) curves, (c) coercivity, (d) remanence and (e) magnetic saturation for the exchange-coupled (100 − x)% Nd–Fe–B/x% Fe–Co nanocomposites containing different mol% (x) of Fe–Co nanoparticles.

at the grain interfaces of the two (soft and hard) magnetic components. Another likely reason is that when the soft nanoparticles diffuse into the hard phase structure, it increases the crystallinity to a certain degree (Fig. S7†). That might help to enhance the properties of the magnetic materials.

However, when Fe–Co mol% increases further, although the M_s value of the nanocomposite increased gradually as expected, variations in the values of H_c and M_r were not regular (Table 1). As can be noticed in Table 1, the nanocomposites prepared with 7.7 mol% of Fe–Co revealed the highest energy product among all the composites prepared in this work. Although the energy product estimated for the nanocomposite containing the optimum amount of Fe–Co is highest among all the samples, the value is lower than the literature reported energy product values of exchange-coupled nanocomposites such as $Nd_2(Fe,Co)_{14}B$ fabricated using a similar synthetic protocol.[15,16,19] Relatively lower energy product of the exchange-coupled hard–soft nanocomposites fabricated in this work might be due to the diffusion of Co atoms across the grains of the two (soft and hard) phases and low density of the nanocomposite. In Henkel plot (Fig. S11†), the $\delta M(H)$ values of isotropic Nd–Fe–B/Fe–Co composite were observed to be negative, indicating that the dipole interaction between the hard and soft magnetic phases was dominant during the reversal procedure. In addition, two negative peaks were observed in the range of 15 kOe. It means that various magnetic interactions could be occurred between the hard magnetic phases, the hard and soft magnetic phases, the inter-grains, or even inter-particles in these composites.[35–37]

Table 1 Magnetic properties of exchange coupled NdFeB/FeCo nanocomposites prepared with different mol% (x) of FeCo nanoparticles

(100 − x)%Nd–Fe–B/x%Fe–Co	0.0	7.7	26.9	42.3	100
H_c (kOe)	3.9	5.6	3.7	3.3	0.6
M_r (emu g^{-1})	44.0	54.0	52.0	47.0	43.0
M_s (emu g^{-1})	67.0	79.0	83.0	91.0	152.0
$(BH)_{max}$ (MGOe)	2.35	4.27	3.87	2.10	0.61

Conclusions

In summary, an exchange-coupled nanocomposite magnet of $Nd_2Fe_{14}B$/Fe–Co with different soft phase contents could be prepared successfully utilizing sol–gel combustion and reduction–diffusion processes. While the utilization of the appropriate amount of reducing agent CaH_2 in the reduction–diffusion process is critical for the complete elimination of CaO by-product and undesired hydrogenation of the hard phase, the fraction of the soft phase in the nanocomposite determines the extent of particle agglomeration and inter-grain fusion during high-temperature reduction–diffusion treatment. Incorporation of about 7.7 mol% of Fe–Co soft phase in the $Nd_2Fe_{14}B$ hard phase is seen to be optimum for producing the highest exchange energy product $(BH)_{max}$ in the exchange-coupled nanocomposite. Diffusion of Co at the hard–soft interface during the high-temperature reduction–diffusion process seems to have a deteriorating effect on the performance of the exchange-coupled hard–soft nanocomposites.

Author contribution

H. N. designed and conducted experiments, organize data and writing manuscript. G. L. performed and analysed Henkel plot and magnetic properties. K. H. plotted graphs and organized figures. U. P. revised, and edited manuscript writing and data. K. K. performed VSM measurement of Fe–Co. T. H. performed additional experiments. J. K., H. W., Y. K. validated the results. Y. S. Kang supervised the research project and made conclusions. All authors have read and agreed to the published version of the manuscript.

Conflicts of interest

There are no conflicts to declare.

Acknowledgements

This work is financially supported by the Leader Project at the Sogang University funded by the Ministry of Science and ICT through the National Research Foundation of Korea (No. 2020R1A3B3079715). U. P. expresses his sincere thanks to National Research Foundation of Korea, Republic of Korea for its support through Brain Pool Program (Grant #2019H1D3A2A01059781). We thank Sung-woo Lee at the Center for Research Facilities, Chungnam National University for PPMS measuring, Ji-Hye Kim at Research Facilities center, Sungkyunkwan University, Yoon-Hee Lee at KCAP, Sogang University for TEM measuring, Ji-Hye Yoo at Sogang LINC for SEM measuring.

References

1 N. Poudyal and J. P. Liu, *J. Phys. D: Appl. Phys.*, 2013, **46**, 043001.
2 S. K. Haider, M.-C. Kang, J. Hong, Y. S. Kang, C.-W. Yang and D. Kim, *Sci. Rep.*, 2021, **11**, 6347.
3 S. K. Haider, J.-Y. Lee, D. Kim and Y. S. Kang, *ACS Sustainable Chem. Eng.*, 2020, **8**, 8156–8163.
4 S. K. Haider, H. M. Ngo, D. Kim and Y. S. Kang, *Sci. Rep.*, 2021, **11**, 10063.
5 R. Skomski and J. M. Coey, *Phys. Rev. B: Condens. Matter Mater. Phys.*, 1993, **48**, 15812–15816.
6 B. Balamurugan, D. J. Sellmyer, G. C. Hadjipanayis and R. Skomski, *Scr. Mater.*, 2012, **67**, 542–547.
7 E. F. Kneller and R. Hawig, *IEEE Trans. Magn.*, 1991, **27**, 3588–3600.
8 J. M. D. Coey and R. Skomski, *Phys. Scr.*, 1993, **T49a**, 315–321.
9 E. E. Fullerton, J. S. Jiang and S. D. Bader, *J. Magn. Magn. Mater.*, 1999, **200**, 392–404.
10 J. M. D. Coey, *IEEE Trans. Magn.*, 2011, **47**, 4671–4681.
11 W. B. Cui, Y. K. Takahashi and K. Hono, *Adv. Mater.*, 2012, **24**, 6530–6535.
12 Y. Hou, S. Sun, C. Rong and J. P. Liu, *Appl. Phys. Lett.*, 2007, **91**, 153117.
13 B. Shen, A. Mendoza-Garcia, S. E. Baker, S. K. McCall, C. Yu, L. Wu and S. Sun, *Nano Lett.*, 2017, **17**, 5695–5698.
14 L. Yu, C. Yang and Y. Hou, *Nanoscale*, 2014, **6**, 10638–10642.
15 Y. Zhong, V. Chaudhary, X. Tan, H. Parmar and R. V. Ramanujan, *J. Alloys Compd.*, 2018, **747**, 755–763.
16 Y. Zhong, V. Chaudhary, X. Tan, H. Parmar and R. V. Ramanujan, *Nanoscale*, 2017, **9**, 18651–18660.
17 W. B. Cui, S. J. Zheng, W. Liu, X. L. Ma, F. Yang, Q. Yao, X. G. Zhao and Z. D. Zhang, *J. Appl. Phys.*, 2008, **104**, 053903.
18 C. B. Rong, D. Wang, V. V. Nguyen, M. Daniil, M. A. Willard, Y. Zhang, M. J. Kramer and J. P. Liu, *J. Phys. D: Appl. Phys.*, 2013, **46**, 045001.
19 M. Yue, X. Zhang and J. P. Liu, *Nanoscale*, 2017, **9**, 3674–3697.
20 G. S. Chaubey, N. Poudyal, Y. Z. Liu, C. B. Rong and J. P. Liu, *J. Alloys Compd.*, 2011, **509**, 2132–2136.
21 D. Jiles, *Introduction to Magnetism and Magnetic Materials*, CRC Press, NewYork, 3rd Edition edn, 2015.
22 G. S. Chaubey, C. Barcena, N. Poudyal, C. Rong, J. Gao, S. Sun and J. P. Liu, *J. Am. Chem. Soc.*, 2007, **129**, 7214–7215.
23 S.-M. Verónica, L. M. Liz-Marzan and M. Farle, *Langmuir*, 2004, **20**, 6946–6950.
24 A. E. Danks, S. R. Hall and Z. Schnepp, *Mater. Horiz.*, 2016, **3**, 91–112.
25 H. Parmar, T. Xiao, V. Chaudhary, Y. Zhong and R. V. Ramanujan, *Nanoscale*, 2017, **9**, 13956–13966.
26 P. K. Deheri, V. Swaminathan, S. D. Bhame, Z. W. Liu and R. V. Ramanujan, *Chem. Mater.*, 2010, **22**, 6509–6517.
27 H. X. Ma, C. W. Kim, D. S. Kim, J. H. Jeong, I. H. Kim and Y. S. Kang, *Nanoscale*, 2015, **7**, 8016–8022.
28 H. Rahimi, A. Ghasemi, R. Mozaffarinia and M. Tavoosi, *J. Magn. Magn. Mater.*, 2017, **444**, 111–118.
29 A. P. Jadhav, A. Hussain, J. H. Lee, Y. K. Baek, C. J. Choi and Y. S. Kang, *New J. Chem.*, 2012, **36**, 2405–2411.
30 S. J. Schneider, *NBS Monograph: Compilation of the Melting Points of the Metal Oxides*, US National Bureau of Standards, Washington, D.C, 1963.
31 C. W. Km, Y. H. Km, H. G. Cha and Y. S. Kang, *Phys. Scr.*, 2007, **T129**, 321–325.
32 C. W. Kim, Y. H. Kim, U. Pal and Y. S. Kang, *J. Mater. Chem. C*, 2013, **1**, 275–281.
33 J. H. Jeong, H. X. Ma, D. Kim, C. W. Kim, I. H. Kim, J. W. Ahn, D. S. Kim and Y. S. Kang, *New J. Chem.*, 2016, **40**, 10181–10186.
34 X. Tan, H. Parmar, Y. Zhong, V. Chaudhary and R. V. Ramanujan, *IEEE Magn. Lett.*, 2017, **8**, 1–5.
35 K. W. Geng, F. Pan and R. H. Yao, *J. Appl. Phys.*, 2008, **104**, 073902.
36 T. Maurer, F. Zighem, W. Fang, F. Ott, G. Chaboussant, Y. Soumare, K. A. Atmane, J.-Y. Piquemal and G. Viau, *J. Appl. Phys.*, 2011, 110.
37 F. Wang, G. Tang, B. Bian, L. Yao, Y. Liu, Q. Zheng and J. Du, *J. Rare Earths*, 2020, **38**, 84–89.